Published in final edited form as:

ACS Appl Mater Interfaces. 2021 December 15; 13(49): 58401–58410. doi:10.1021/acsami.1c18941.

Effect of Nanoparticle Synthetic Conditions on Ligand Coating Integrity and Subsequent Nano-Biointeractions

Jessica C. Hsu,
Department of Radiology, University of Pennsylvania, Philadelphia, Pennsylvania 19104, United States; Department of Bioengineering, University of Pennsylvania, Philadelphia, Pennsylvania 19104, United States

Yu Du,
Division of Gastroenterology and Hepatology, University of Pennsylvania, Philadelphia, Pennsylvania 19104, United States

Arjun Sengupta,
Department of Systems Pharmacology and Translational Therapeutics, University of Pennsylvania, Philadelphia, Pennsylvania 19104, United States

Yuxi C. Dong,
Department of Radiology, University of Pennsylvania, Philadelphia, Pennsylvania 19104, United States; Department of Bioengineering, University of Pennsylvania, Philadelphia, Pennsylvania 19104, United States

Katherine J. Mossburg,
Department of Radiology, University of Pennsylvania, Philadelphia, Pennsylvania 19104, United States; Department of Bioengineering, University of Pennsylvania, Philadelphia, Pennsylvania 19104, United States

Mathilde Bouché,
Department of Radiology, University of Pennsylvania, Philadelphia, Pennsylvania 19104, United States

Andrew D. A. Maidment,
Department of Radiology, University of Pennsylvania, Philadelphia, Pennsylvania 19104, United States

Aalim M. Weljie,
Department of Systems Pharmacology and Translational Therapeutics, University of Pennsylvania, Philadelphia, Pennsylvania 19104, United States

Corresponding Author: David P. Cormode – Department of Radiology, University of Pennsylvania, Philadelphia, Pennsylvania 19104, United States; Department of Bioengineering, University of Pennsylvania, Philadelphia, Pennsylvania 19104, United States; Phone: 215-615-4656; david.cormode@uphs.upenn.edu; Fax: 215-662-7868.

Supporting Information

The Supporting Information is available free of charge at https://pubs.acs.org/doi/10.1021/acsami.1c18941.

Energy dispersive X-ray spectroscopy spectrum, UV–visible spectroscopy measurements, 2D NMR spectroscopy, in vivo 3D volume rendered CT images, electron micrographs of liver sections, and flow cytometry of primary Kupffer cells (PDF)

The authors declare no competing financial interest.

David P. Cormode
Department of Radiology, University of Pennsylvania, Philadelphia, Pennsylvania 19104, United States; Department of Bioengineering, University of Pennsylvania, Philadelphia, Pennsylvania 19104, United States

Abstract

Most current nanoparticle formulations have relatively low clearance efficiency, which may hamper their likelihood for clinical translation. Herein, we sought to compare the clearance and cellular distribution profiles between sub-5 nm, renally-excretable silver sulfide nanoparticles (Ag_2S-NPs) synthesized via either a bulk, high temperature, or a microfluidic, room temperature approach. We found that the thermolysis approach led to significant ligand degradation, but the surface coating shell was unaffected by the microfluidic synthesis. We demonstrated that the clearance was improved for Ag_2S-NPs with intact ligands, with less uptake in the liver. Moreover, differential distribution in hepatic cells was observed, where Ag_2S-NPs with degraded coatings tend to accumulate in Kupffer cells and those with intact coatings are more frequently found in hepatocytes. Therefore, understanding the impact of synthetic processes on ligand integrity and subsequent nano-biointeractions will aid in designing nanoparticle platforms with enhanced clearance and desired distribution profiles.

Graphical Abstract

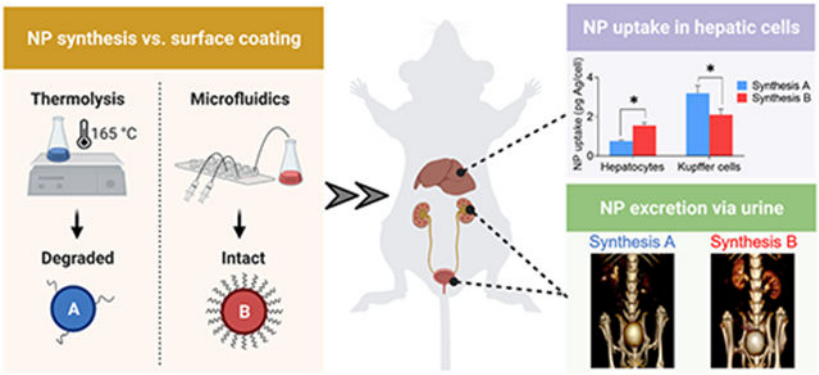

Keywords

nanoparticles; microfluidics; renal clearance; silver sulfide; hepatic cells

INTRODUCTION

Synthetic control over a nanoparticle's physicochemical properties, such as size and surface chemistry, can determine its biodistribution and pharmacokinetics among other factors.[1,2] For example, nanoparticles are often modified with long hydrophilic polymer ligands, such as polyethylene glycol (PEG), for imaging the vasculature, atherosclerotic plaques, and tumors due to increased blood circulation times.[3-5] However, nanoparticles that do not undergo renal filtration are eventually cleared from the circulation by phagocytic cells in the reticuloendothelial system (RES) organs, namely, the liver and spleen. Some nanoparticles

may be further catabolized through hepatocytes in the liver and eliminated in feces via the biliary system. Hepatobiliary excretion of nanoparticles can be very slow, ranging from hours to months after administration. Thus, prolonged accumulation of nanoparticles in the phagocytes and liver parenchyma may lead to possible longterm toxicity, especially for nondegradable formulations that contain heavy metal elements.[6] Concerns over the retention of such agents remain a major challenge for translation.

Many reports have focused on the development of renally-clearable nanoparticles that can be rapidly eliminated via the urine, thus reducing uptake by the RES organs.[7-10] Glomeruli in the renal cortex of the kidneys are mainly responsible for the urinary excretion of intravenous nanoparticle agents. The glomerular filtration barrier is consisted of multiple cell layers, each with a distinct pore size and charged surface.[11] In general, nanoparticles smaller than 6 nm and capped with neutral surface ligands, such as glutathione, undergo renal excretion within minutes to hours after administration.[12] We recently reported the successful clearance of sub-5 nm silver sulfide nanoparticles (Ag_2S-NPs) via urine with low accumulation in the RES organs.[13] Importantly, we found that 85% of the injected dose (ID) was excreted within 24 h of intravenous injection, whereas only 20–75% of ID is cleared for most renally excreted nanoparticle formulations.[14] Furthermore, the clearance did not greatly improve at longer time points for these prior formulations.[15,16] Despite the relatively extensive clearance that we observed for Ag_2S-NPs, better excretion is needed for clinical translation. We hypothesized that the glutathione ligands used as surface coatings might be degraded during the nanoparticle formation process, especially in the case of thermolysis of molecular precursors as in the previously used synthesis. For more efficient renal clearance, the surface ligands should remain intact in order to carry out their functions of providing stability in biological media, deterring protein adsorption, and avoiding sequestration from phagocytic cells.[17] We therefore sought to understand the effects of synthetic conditions on coating ligand integrity and subsequent clearance and nano-biointeractions of Ag_2S-NPs.

In this study, we developed a novel microfluidic approach to synthesize sub-5 nm Ag_2S-NPs, while preserving the glutathione ligands during the process. This synthesis prevents the decomposition of organic coatings by introducing a primary sulfur source and allowing nanoparticle formation to proceed at room temperature. As a result, the structure of the surface coating shell of the as-synthesized Ag_2S-NPs remained unchanged, as determined by nuclear magnetic resonance (NMR) spectroscopy and thermogravimetric analysis (TGA). In vivo CT imaging showed higher contrast in the kidneys and bladder after injection, indicating the successful renal excretion of these nanoparticles. The clearance of nanoparticles was improved mostly by reducing the level of uptake in the liver. Interestingly, more nanoparticles with intact coatings were found in hepatocytes, indicating the ability to evade Kupffer cells and access the hepatobiliary clearance pathway. Consequently, the findings from this study should advance our knowledge on methods for improving the clearance efficiency and cellular interactions of nanoparticles.

MATERIALS AND METHODS

Materials.

Silver nitrate ($AgNO_3$, 99%), L-glutathione (GSH, 98%), calcium chloride dihydrate, sodium hydroxide solution (NaOH, 1 N), collagenase from *Clostridium histolyticum* (type IV), and deuterium oxide (D_2O, 99.9%) were purchased from Sigma-Aldrich (St. Louis, MO). Anhydrous sodium sulfide (Na_2S) was purchased from Alfa Aesar (Tewksbury, MA). Hank's Balanced Salt Solution (HBSS) buffer (1×) without calcium, magnesium, and phenol red was purchased from Invitrogen (Waltham, MA). EGTA buffer (0.5 M, pH 8) was purchased from Fisher Scientific (Pittsburgh, PA). OptiPrep density gradient medium (60% iodixanol in water) was purchased from BioVision Inc. (Milpitas, CA). An Insyte Autoguard shielded IV catheter (24G × 0.75") and ethylene glycol were purchased from Becton, Dickinson and Company (Franklin Lakes, NJ). PE-conjugated monoclonal anti-F4/80 antibodies were purchased from Miltenyi Biotec (Bergisch Gladbach, North Rhine-Westphalia, Germany). Herringbone microfluidic chip mixers and male luer fluid connectors were purchased from Microfluidic ChipShop (Jena, Germany).

Synthesis of Ag_2S-NPs via Thermal Decomposition of Single-Source Precursors.

We synthesized hydrophilic Ag_2S-NPs with size tunability according to our previous report.[13] Briefly, $AgNO_3$ (100 mg) and GSH (140 mg) were added to ethylene glycol (40 mL), which was preheated to 120 °C. The mixture was purged with nitrogen gas and heated at a rate of 20 °C per minute up to 165 °C. Different nanoparticle core sizes were obtained by quenching the reaction in ice water at various time points. The products were isolated by centrifuging (7000 rcf for 10 min) with absolute ethanol. The collected pellet was resuspended in DI water and washed thrice (centrifuging at 4000 rpm for 30 min) using 3000 Da MWCO filtration tubes (Sartorius Stedim Biotech, Germany). The buffer was changed to phosphate buffered saline (PBS) after the last wash, and the nanoparticles were filtered through a 0.02 μm membrane (GE Healthcare Life Sciences, UK) and stored at 4 °C for subsequent experiments.

Synthesis of Ag_2S-NPs via a Novel Microfluidic Approach.

We developed a novel microfluidic method to synthesize water-soluble, low dispersity Ag_2S-NPs with tunable core sizes using glutathione as the surface coating ligand. First, 767 mg of GSH (2.5 mmol) was added to a flask containing 75 mL of DI water while stirring and the pH of the mixture was adjusted to 7.5 using NaOH; 42.5 mg of $AgNO_3$ (0.25 mmol) was then added to the same mixture and the pH was again adjusted to 7.5 using NaOH. The resulting solution, which was clear and colorless, was loaded in a 10 mL syringe. In a separate flask, 10 mg of Na_2S (0.13 mmol) was dissolved in 25 mL of DI water while stirring and the solution was loaded in a 10 mL syringe. The final molar ratios of GSH (ligand):$AgNO_3$ (silver precursor) and $AgNO_3$ (silver precursor):Na_2S (sulfur source) were 10:1 and 2:1, respectively. Next, the syringes were mounted onto syringe pumps, and both solutions were injected into a herringbone microfluidic chip mixer.[1820] To synthesize nanoparticles with different core sizes, the flow rate for the Na_2S solution was fixed at 0.5 mL/min and the flow rate for the GSH/$AgNO_3$ solution was varied between 0.5 and 2.5 mL/min. The resultant mixture was collected in a flask, covered in aluminum foil, and subjected

to constant stirring for 24 h under ambient conditions. The nanoparticle suspension, which was dark brown in color, was washed three times in DI water and concentrated to a final volume of 1 mL using 3000 Da MWCO filtration tubes. The tubes were spun for 20 min at 4000 rpm. Any aggregates in the suspension were removed by a 0.02 μm membrane. The final product was stored at 4 °C.

Nanoparticle Characterization.

The core sizes and morphologies of Ag_2S-NPs were examined using a Tecnai T12 transmission electron microscope (FEI, Hillsboro, OR) operating at 100 kV. The elemental content of Ag_2S-NPs was assessed using an FEI Quanta 600 scanning electron microscope (FEI, Hillsboro, OR) equipped with EDAX EDS detectors (Ametek, Mahwah, NJ). The elemental silver concentrations were measured by inductively coupled plasma–optical emission spectrometry (ICP-OES, Spectro Genesis, Germany) following digestion in nitric acid and dilution with DI water. The hydrodynamic diameter and surface zeta potential of Ag_2S-NPs (concentration of 0.1 mg of Ag per mL) were assessed using a Nano-ZS-90 Zetasizer (Malvern Instruments, UK). ^{1}H, ^{1}H-^{1}H COSY, and ^{1}H-^{13}C HSQC spectra of Ag_2S-NP samples suspended in D_2O were recorded at room temperature on a Bruker DMX 500 NMR spectrometer equipped with 5 mm dual (^{1}H/^{13}C) z-gradient probe heads using the residual solvent peak as a reference. The thermal behavior of Ag_2S-NP samples was examined by thermogravimetric analysis (TGA) using an SDT Q600 TGA instrument (TA Instruments, New Castle, DE) with a weight sensitivity of 0.1 μg. The instrument was purged with nitrogen gas at a flow rate of 100 mL/min and was heated up to 500 °C at a rate of 20 °C/min. An average of 10 mg of the solid sample was used for the TGA experiment. Data are presented as mean ± standard deviation (SD).

Animals.

All animal experiments were performed using female nude mice (8 weeks old, n = 4 per group) purchased from the Jackson Laboratory (Bar Harbor, Maine). Isoflurane was used to induce anesthesia in mice. All experimental protocols were approved by the Institutional Animal Care and Use Committee at University of Pennsylvania.

Biodistribution.

In brief, mice were sacrificed at 24 h after injection. Blood samples were collected before perfusion with PBS. Major tissues including the bladder, feces, lungs, liver, heart, spleen, and kidneys were collected and their weights were recorded. Next, they were finely minced and subjected to overnight digestion with nitric acid (3 mL) at 75 °C. Then, each sample was added with 7 mL of DI water and filtered with a 0.22 μm membrane prior to ICP-OES analyses. Data are presented as mean ± standard error of mean (SEM).

In Vivo CT Imaging.

In vivo CT images were acquired with a MILabs μCT scanner (Utrecht, The Netherlands) using the following parameters: peak voltage = 50 kV, current = 240 μA, step angle = 0.75°, and exposure time = 75 ms. Mice were injected via the tail vein with Ag_2S-NPs suspended in PBS at a dose of 250 mg Ag/kg. The mice were scanned before injection and at 5, 30, 60,

and 120 min post-injection. The acquired images were subsequently analyzed with OsiriX. The change in CT attenuation from preinjection scan of each tissue type is presented as mean ± SEM in Hounsfield units.

Examination of Liver Tissue via TEM.

Treated liver tissue samples were fixed in 2.5% glutaraldehyde and 2% paraformaldehyde and then stained and embedded. Samples in 60 nm thick sections were mounted onto copper grids and viewed using a Tecnai T12 electron microscope operated at 100 kV.

Isolation of Hepatocytes and Kupffer Cells.

Hepatocytes and Kupffer cells were isolated from livers of treated mice following a literature method with some modifications.[21,22] First, solutions for liver perfusion and cell isolation were prepared using DI water and stored at 4 °C unless otherwise specified. HBSS-EGTA buffer (0.5 mM) was prepared by mixing 500 μL of EGTA with 500 mL of HBSS. HBSS-$CaCl_2$ buffer (1 mM) was prepared by mixing 500 μL of 1 M $CaCl_2$ with 500 mL of HBSS. Concentrated collagenase solution was prepared by adding 1.6 g of collagenase to 50 mL of HBSS-$CaCl_2$ buffer. This solution was filtered through a 0.45 μm membrane and stored at −20 °C as 1 mL aliquots. One milliliter of concentrated collagenase solution was thawed just before use and added to 49 mL of HBSS-$CaCl_2$ buffer. All reagents were heated to 37 °C in a water bath prior to the procedure. A silicone tubing was passed through a FH100M multichannel peristaltic pump (Fisher Scientific, Hampton, NH) that was set at a volumetric flow rate of 4 mL/min. One end of the tubing was connected to a catheter needle and the other end was immersed in warm HBSS-EGTA buffer.

Next, mice were anesthetized with isoflurane and placed on their back on a dissection board. Their limbs were secured to the board and the abdomen was sanitized with ethanol wipes. Then, an incision was made on the ventral midline and the skin was dissected away. The peritoneal cavity was exposed, and the intestines were pushed to the side using a cotton tip. A catheter needle was inserted into the hepatic portal vein, and the pump was immediately activated. The inferior vena cava was cut when the liver became swollen and discolored. The liver was perfused with the buffer for 5 min after which the tubing was transferred to the collagenase solution. The liver was then digested with collagenase for 5 min. Cell release and lobe breakdown were observed during this time. After the digestion process was complete, the entire liver was dissected and placed in a Petri dish with cold HBSS-$CaCl_2$ buffer. The hepatic cells were released by gently mincing the liver lobes until no clumps were visible and were filtered through a 100 μm cell strainer with additional cold HBSS-$CaCl_2$ buffer.

The filtered cells were collected in a 50 mL centrifuge tube and spun at 50 rcf for 3 min at 4 °C. The pellet, which contained only hepatocytes, was washed and purified three times with HBSS-$CaCl_2$ buffer using the same centrifugation condition. The supernatant, which consisted of nonparenchymal cells (i.e., Kupffer cells, endothelial cells, and stellate cells), were spun at 500 rcf for 8 min at 4 °C. After the centrifugation spin was complete, the pellet was collected and resuspended in 3 mL of 24% OptiPrep solution (i.e., 10 mL of OptiPrep stock was diluted with 15 mL of DMEM culture medium). The cell fraction was placed at

the bottom of a 15 mL centrifuge tube, while 3 mL of 17.6% OptiPrep solution (i.e., 10 mL of OptiPrep stock diluted with 24 mL of DMEM) was loaded on top of the cell suspension. Another layer was created by loading 3 mL of 11.2% OptiPrep solution (i.e., 10 mL of OptiPrep stock was diluted with 43.5 mL of DMEM) on top of the 17.6% OptiPrep layer. Then, 3 mL of DMEM culture medium was loaded on top of all three layers. Extra care should be taken when creating the density gradient layers to avoid mixing at the interphases. The mixture was spun at 1400 rcf for 18 min without brakes after which the cell fraction between the 11.2 and 17.6% Optiprep layers was collected. This cell suspension, enriched with Kupffer cells and liver sinusoidal endothelial cells (LSEC), was washed and purified three times with PBS by centrifuging at 500 rcf for 10 min. Purified hepatocytes and Kupffer cells were fixed with 4% paraformaldehyde for 15 min at room temperature and then washed with PBS. The cell fractions were suspended in PBS and stored at 4 °C for further analyses.

Analysis of Silver Content in Hepatic Cells.

Hepatocytes and Kupffer cells were manually counted with a hemocytometer and spun down to form a pellet. Cell pellets were subjected to overnight digestion in 1 mL of nitric acid at 75 °C. Each digested sample was diluted with 3 mL of DI water and filtered through a 0.45 μm membrane to remove cell debris. Finally, the silver content in each sample was analyzed via ICP-OES. Data are presented as mean ± SEM.

Flow Cytometry.

The purity of the suspension containing Kupffer cells and LSEC was analyzed using flow cytometry; 10^8 cells in 95 μL of PBS were incubated with 5 μL of PE-conjugated recombinant human-anti-mouse F4/80 monoclonal antibodies (i.e., a major macrophage marker) for 20 min at 4 °C in the dark. Cells were then washed three times with PBS to remove excess antibody–dye conjugates. Flow cytometry was performed using a FACSCanto System (BD Sciences, San Jose, CA). The results were analyzed using the FlowJo version 9 software.

Statistics.

All studies included at least three replicates or three independent experiments. All statistical analyses were performed using GraphPad Prism 8 software. The figure caption recorded the specific statistical tests that were done, when applicable.

RESULTS

Novel Microfluidic Synthesis Maintains the Ligand Structure.

Ag_2S-NPs were synthesized either via a one-pot, high temperature (Synthesis A), or a microfluidic, room temperature (Synthesis B) approach. As reported in our previous study,[13] Synthesis A involves the heating of silver nitrate and glutathione in ethylene glycol and quenching the reaction at different time points. Silver nitrate served as the Ag^+ source and glutathione functioned as both the capping ligand and sulfur donor.[23] Glutathione consists of several functional groups, such as –SH, –COOH, and $–NH_2$, which strongly coordinate with transition metal ions,[24,26] forming high affinity metal–ligand clusters. Upon mixing of silver nitrate and glutathione, glutathione would chelate with Ag^+ to form the initial Ag-thiolate

precursor complexes.[27] Then, heat was applied to the reaction mixture. During this process, the carbon–sulfide (C—S) bonds were cleaved as Ag-thiolate complexes decompose due to high temperature.[28-30] As a result, Ag_2S nuclei began to form and continued to grow until the sulfur source was depleted or the reaction was quenched. In our previous report, we quenched the reaction between 10 and 20 min to obtain an array of Ag_2S-NPs with core sizes ranging between 2 and 7 nm (Figure 1A), as determined by transmission electron microscopy (TEM). For Ag_2S-NPs with a core diameter of 3.1 nm, the hydrodynamic diameter (HD) and surface zeta potential were found to be 4.9 ± 1.0 nm and −11 ± 2 mV, respectively.

A novel microfluidic approach (Synthesis B) was developed to synthesize Ag_2S-NPs under ambient conditions, while introducing a separate sulfur source. In this synthesis, we mixed glutathione with silver nitrate in water and raised the pH of the solution to near neutrality, thus allowing glutathione molecules to coordinate Ag^+ with high selectivity.[31] This mixture, which contains initial Ag-glutathione complexes, was injected along with a solution of sodium sulfide into a herringbone microfluidic chip mixer that creates repeated rotational and extensional flows to efficiently and homogeneously mix the input streams.[32] Silver nitrate and glutathione served as the sources of silver ions and capping ligands, respectively. Sodium sulfide functioned as the primary donor of sulfide ions. As described in other reports, the nucleation of Ag_2S nuclei was triggered by the addition of in_organic sulfide to the preformed Ag-glutathione complexes.[33-35] Then, the free thiol groups of glutathione would bind to the surface of the nanoparticles as the Ag_2S cores were formed. The nanocrystal growth was controlled by varying the combined flow speeds. For example, the combined speed was varied between 1 and 3 mL/min to obtain an array of Ag_2S-NPs with core sizes ranging between 2 and 7 nm (Figure 1B), as determined by TEM. For Ag_2S-NPs with a core diameter of 3.2 nm, HD and surface zeta potential were found to be 4.8 ± 0.2 nm and −6.3 ± 1.7 mV, respectively. These nanoparticles have a 1:2 S:Ag stoichiometry (Figure S1) and are stable under physiological conditions (Figure S2).

Next, we analyzed the ligand structure and surface chemistry of 3 nm Ag_2S-NPs obtained from Synthesis A and Synthesis B using one-dimensional ^1H NMR spectroscopy. The NMR spectrum of Ag_2S-NPs obtained from Synthesis A is shown in Figure 2 (middle). We observed no obvious proton resonance peaks or chemical shifts that correspond to glutathione molecules (Figure 2, top). Hence, there must be a variety of ligand species (likely glutathione degradation products) on the nanoparticle surface. On the other hand, the NMR spectrum of Ag_2S-NPs obtained from Synthesis B is shown in Figure 2 (bottom), which is more comparable to that of free glutathione molecules (Figure 2, top). Some protons, such as those attached to C3 and C11, showed proton chemical shifts upfield and resonance broadening due to hydrogen bonding between molecules.[36] Moreover, the two geminal protons attached to C8 (i.e., in the α-position to the thiol group and metal core) showed a signal splitting in two multiplets and significant downfield deshielding of only one of these protons. This indicates that the geminal protons in the α-position to the thiol experience different chemical environments due to diaster-eotopicity induced by the chiral metal core.[37,38] Moreover, the proton attached to C7 showed chemical shift downfield, which is influenced by the chiral carbon. We also performed twodimensional ^1H-^1H COSY and ^1H-^{13}C HSQC NMR spectroscopy of Ag_2S-NPs obtained from Synthesis B (Figure S3).

The two geminal protons on C8 indeed appear as two distinct multiplets according to the HSQC spectrum. These results further confirm the binding of glutathione molecules to the Ag_2S-NP surface and demonstrate that the structure of the coating ligand was not impacted by the synthetic conditions of the microfluidic approach.

The top spectrum represents the ^1H resonances of free glutathione ligands. The middle and bottom spectra represent the ^1H resonances of Ag_2S-NPs produced from Synthesis A and Synthesis B, respectively. Circles indicate a proton signal splitting that is induced by the nearby chiral carbon (C8).

We then performed TGA to investigate the presence and amount of surface-bound organic ligands. The silver sulfide cores have a melting point of 825 °C, which is beyond the temperature range used for the analysis and thus should not contribute to the weight change (%). As shown in Figure 3, we found a small change in the weight change (<0.04%/°C) of Ag_2S-NPs obtained from Synthesis A (blue curve), indicating that a small amount of organic material is present in the nanoparticle sample. On the other hand, we found the weight change per Celsius degree of Ag_2S-NPs obtained from Synthesis B (red curve) to follow a similar trend as glutathione (black curve), while having a lower overall decrease. Several thermal degradation steps in the TGA curve can be found due to the decomposition of the organic molecules.[39] The largest weight change occurred around 200 °C, which corresponds to the melting point and decomposition of glutathione. At the max temperature of 500 °C, the total mass loss in Ag_2S-NPs from Synthesis B amounts to 33 wt %, which is much higher than that of Ag_2S-NPs from Synthesis A (10.5 wt %). From these results, we determined that the one-pot, high temperature synthesis (which uses the thiol ligand as the sulfur donor) can compromise the integrity of nanoparticle surface coatings. We also demonstrated that the microfluidics, room temperature approach (using a separate sulfur donor) can preserve the structural integrity of glutathione ligands.

CT Imaging Indicates Fast Renal Clearance of Ag_2S-NPs with Intact Ligands.

We have previously shown Ag_2S-NPs to provide CT contrast.[13,40] We herein monitored the clearance potential of Ag_2S-NPs using a small animal μCT scanner. We found that Ag_2S-NPs with degraded ligands (from Synthesis A) were cleared through the kidneys into the bladder after injection to a significant degree (Figure S4).[13] A similar effect was observed for Ag_2S-NPs with intact ligands (from Synthesis B). As shown in Figure 4A, both the kidneys and bladder showed higher CT contrast after injection. The three main internal regions of the kidneys, including the cortex (which contains glomeruli that filter nanoparticles), medulla, and pelvis, were well distinguished at 5 min post-injection. Filtration and excretion of these nanoparticles were evident in the segmented data (using a 3D region growing method), where the cortex and ureter were shown in detail (Figure 4B). The kidney contrast gradually decreased, whereas the contrast in the RES organs remained at a slightly higher level (<65 HU) than preinjection (Figure 4C). Interestingly, we observed a faster renal clearance rate with nanoparticles from Synthesis B, as evidenced by the strong contrast in the kidneys and less contrast in the blood immediately after injection (Figure 4D). Therefore, tracking nanoparticle clearance with CT imaging revealed that the integrity

of surface coating ligands can greatly influence the excretion rate and pharmacokinetics of inorganic nanoparticles.

Intact Surface Coating Improves Clearance by Reducing Liver Uptake.

We determined the impact of surface coating integrity on the biodistribution profiles. At 24 h after injection, we used ICP-OES to analyze the silver content in major organs. In particular, we found the retention of silver in the liver to be statistically significantly different between the two nanoparticle formulations (Figure 5A). The liver uptake of Ag_2S-NPs with degraded coatings (9.53 ± 0.5% ID) was nearly twofold higher than Ag_2S-NPs with intact coatings (4.96 ± 1.3% ID). We calculated a clearance efficiency of 87.9 ± 0.4% ID and 92.5 ± 1.7% ID for 3 nm Ag_2S-NPs with degraded and intact surface ligands, respectively. Silver uptake in other organs was not statistically significantly different between the two Ag_2S-NP formulations. Hence, the structural integrity of surface ligands plays a role in the clearance of nanoparticles, where the intact coating shell improves clearance by reducing the uptake in the liver.

Differential Nanoparticle Distribution in Hepatic Cells due to Coating Integrity.

Based on the biodistribution results, we examined the liver uptake between the two Ag_2S-NP formulations by qualitatively inspecting the liver tissues under TEM and quantitatively analyzing for their silver content via ICP-OES. Inspecting these liver sections under TEM revealed that Ag_2S-NPs from Synthesis A (with degraded coating) were mostly located in Kupffer cells, while Ag_2S-NPs from Synthesis B (with intact coating) were frequently found in the hepatocytes with some distributed in the Kupffer cells (Figure S5). Hence, the distribution of nanoparticles was shifted to hepatocytes upon maintaining the integrity of surface ligands.

Next, we isolated primary hepatic cells and analyzed for their silver content. Hepatocytes are denser than other liver cell types and thus can be easily pelleted and separated from the rest of the cell suspension using low centrifugation speeds.[41] Purified nonparenchymal cells, such as Kupffer cells and LSEC, were examined with flow cytometry. Cells were incubated with PE-conjugated anti-F4/80 antibodies. After gating the flow cytometry data, we found the ratio of $F4/80^+$ (Kupffer cells) and $F4/80^-$ (LSEC) cells in the purified cell fraction to be 1:2 (Figure S6), which is consistent with that observed in vivo.[42] As shown in Figure 5B, silver uptake in the hepatocytes was statistically significantly higher for Ag_2S-NPs with intact coatings (1.55 ± 0.15 pg Ag per cell) compared to Ag_2S-NPs with degraded coatings (0.76 ± 0.05 pg Ag per cell). However, the opposite trend was observed for the Kupffer cell population. This finding is in alignment with the results observed from qualitative measurements with TEM. We determined that the structural integrity of nanoparticle surface ligands has a profound effect on the cellular interactions in vivo, thus resulting in differential hepatic cell distribution profiles.

DISCUSSION

In this study, we hypothesized that the synthetic conditions may affect the integrity of ligands and therefore impact subsequent clearance and biointeractions. As we described

above, Synthesis A, which represents a thermolysis approach, resulted in Ag_2S-NPs with highly degraded surface ligands. This is mainly due to the dissociation of carbon–sulfide bonds of glutathione molecules at high temperature to supply S^{2-} for nanocrystal nucleation and growth. It may be possible to increase the concentration of glutathione, where excess thiol groups may bind to the surface of Ag_2S-NPs. However, this can change the reaction process, since a high glutathione concentration, or rather a low Ag^+ concentration, may lead to fewer nanocrystal seeds and thus larger nanoparticle size, which is not ideal for achieving efficient renal clearance.[29] On the other hand, Synthesis B, which represents a novel microfluidic method, resulted in Ag_2S-NPs with intact coating ligands on the surface. We designed the synthesis to include a primary sulfur donor (i.e., sodium sulfide), thus allowing the reaction to occur at room temperature. In this case, the reagents are not subjected to heating, which may help to maintain the structural integrity of glutathione ligands. Thus, synthetic processes can greatly alter the ligand structures and the resulting nanoparticle surface chemistry and physicochemical properties. To the best of our knowledge, we are the first to report the synthesis of ultrasmall semiconductor nanoparticles based on Ag_2S using a simple microfluidic device. Unlike previously established microfluidic metallic nanoparticle synthesis, our method does not involve complex protocols, specialized equipment, or harsh reaction conditions.[43] Notably, the staggered herringbone micromixer employed in our study has previously been used for generating organic nanomaterial formulations (e.g., lipid and polymeric nanoparticles).[44] Therefore, our work not only demonstrates the versatility and broad applicability of this chip type but also expands the microfluidic synthetic strategies for synthesizing inorganic nanomaterials, especially nontoxic (i.e., free of lead and cadmium) semiconductor nanoparticles.

Next, we closely examined the impact on subsequent clearance and nano-biointeractions due to the difference in ligand integrity. Renal excretion of nanoparticle agents relies on kidney filtration through the glomerular capillaries, whereas hepatic excretion involves transport through the hepatobiliary pathway. Both routes are highly dependent on nanoparticle size and ligand chemistry among other factors.[45] For both Ag_2S-NP formulations, the CT contrast in the bladder was the highest of all organs after injection. Interestingly, Ag_2S-NPs with intact ligands appeared to have a shorter circulation time as less contrast was found in the blood immediately post-injection. Perhaps, the nanoparticle surface is sufficiently coated with zwitterionic functional groups (from intact glutathione) that prevent aggregation and formation of protein corona, thus maintaining a small overall size for optimal renal filterability. This nanoparticle type also yielded a lower retention in the liver. We determined that Ag_2S-NPs with intact ligands are frequently found in the hepatocytes, whereas Ag_2S-NPs with degraded ligands are preferentially located in the Kupffer cells. It should be noted that the silver content measured in Kupffer cell samples also includes the uptake by LSEC. These two cell types were collected from the same cell layer following density gradient centrifugation but were not further separated by flow cytometry sorting. Although LSEC are more abundant than Kupffer cells in the liver, nanoparticles are removed from the circulation more predominantly by the latter.[46] Several studies have suggested that the uptake of nanoparticles by hepatocytes is greatly influenced by the ligand chemistry, such as the degree of PEGylation, peptide conjugation, and surface charge,[47-50] in addition to the nanoparticle size (liver sinusoidal endothelial fenestrations up to 200 nm).[51] Hepatocytes

can further eliminate the nanoparticles through enzymatic breakdown, collection in the bile, and eventual excretion into the intestines and feces.[45] A more detailed schematic and discussion of hepatobiliary clearance can be found in a review article by Zhang et al.[45] This process is rather slow and inefficient compared to swift renal clearance. It is possible that more clearance of nanoparticles, particularly those located in the hepatocytes, would be seen at longer biodistribution time points. However, for nanoparticles to enter hepatocytes, they must first evade Kupffer cells (resident macrophages in the liver) and penetrate the fenestrated endothelium into the space of Disse. Uptake by Kupffer cells is also affected by the surface chemistry. Nanoparticles with negatively charged ligands or low PEG density have been found to accumulate in Kupffer cells.[52-54] Furthermore, nanoparticles that are not degraded by intracellular processes may remain in these cells for months to years and be taken up again by other phagocytes in the liver, resulting in prolonged exposure and potential safety concerns.[55] For example, it was shown that accumulation of some heavy metal nanoparticles in the liver could lead to chronic toxicity, such as fibrosis or changes in gene expression (i.e., upregulation of detoxification pathways).[56] Therefore, the integrity of coating ligands plays a large role in the clearance of nanoparticles as well as the interactions with certain hepatic cell types.

Ag_2S-NPs were reported to be highly stable and biocompatible and were studied as probes for near-infrared fluorescence imaging and photothermal therapy due to their tunable optical properties. Other potential biomedical uses of Ag_2S-NPs have also been reported, including targeted imaging, drug delivery, and biosensing.[57] Recently, we have shown that Ag_2S-NPs generate stronger contrast than iodinated small molecules in dual energy mammography (DEM), a modality that is beneficial for screening breast cancer in women with dense breasts.[40] Compared to conventional imaging probes, nanoparticle agents are particularly suitable for detecting tumors as they are known to carry higher contrast payloads per entity and generate better target to background ratios.[12] To prolong blood residence times and improve tumor accumulation, ultrasmall, renally-clearable nanoparticles could be encapsulated in long-circulating, biodegradable polymeric particles.[19] Our current work, where we have described a novel synthetic approach for producing Ag_2S-NPs with an intact coating shell for greater renal clearance and lower liver uptake, may have a broader impact due to the biomedical applications mentioned above.

In the future, we could investigate the exact nanoparticle distribution between LSEC and Kupffer cells since transcytosis from LSEC to underlying hepatocytes may contribute to more hepatobiliary clearance. We could study the route of uptake for hepatocytes and Kupffer cells to obtain information about other factors that may affect interactions at the cellular level. We could also examine the excreted nanoparticles in the urine via mass spectrometry or liquid chromatography to understand the degree of surface ligand displacement or substitution in vivo. It was reported that the enzymatic degradation of glutathione within the kidneys and efflux of glutathione in the liver sinusoid can modify the nanoparticle surface with endogenous molecules and thus change the overall clearance and biodistribution profiles.[58] Moreover, we could analyze for silver content in the feces to track the hepatobiliary excretion of nanoparticles over several months. We could evaluate the uptake in other phagocytic cell types, such as hepatic B cells or splenic macrophages, to probe how ligand integrity influences the distribution of nanoparticles among different

cellular phenotypes. Lastly, due to apparent differences in the clearance mechanism (e.g., glomerular filtration rate) between humans and mice, similar studies should be performed in larger animal models such as dog or swine to further validate our hypothesis.[59]

CONCLUSIONS

The overall goal of this study is to explore design considerations that are essential for engineering metallic nanoparticles with improved clearance efficiency. More specifically, we investigated the impact of synthetic conditions on nanoparticle surface ligands and the effect of coating integrity on subsequent nanoparticle excretion and distribution. We hypothesized that the inadequate clearance that we observed firsthand (in our previous report) and in current literature may stem from the harsh synthetic conditions that were employed to produce these nanoparticles, which may alter the surface ligands (i.e., glutathione) and thus influence nanoparticle behaviors in vivo. Therefore, we compared the physicochemical properties and clearance of 3 nm Ag_2S-NPs produced from two distinct syntheses (i.e., bulk, high temperature vs microfluidic, room temperature). Herein, we report three key findings that resulted from our work. First, we found that the surface coating integrity of Ag_2S-NPs can be greatly influenced by the synthetic conditions, as indicated by NMR and TGA. Unlike the thermolysis method published in our previous study, the novel microfluidic approach, which we have developed for this work, can maintain the nanoparticle's "synthetic identity"–mainly keeping the surface ligand structure unaltered during the synthesis. Notably, this is the first study to report the use of a staggered herringbone micromixer for synthesizing inorganic nanomaterials with tunable sizes in the aqueous phase and under ambient conditions. Second, we found that an intact surface coating shell can improve the clearance of Ag_2S-NPs by allowing more rapid kidney filtration and significantly reduce the liver uptake by almost twofold, as evidenced by in vivo CT imaging and biodistribution analyses. We observed marked CT contrast of the renal cortex and ureter compared to our previously published CT data. Third, by separating primary hepatic cells via a complex isolation technique and evaluating for their silver content via ICP-OES, we observed a differential nanoparticle distribution in hepatic cell populations. Ag_2S-NPs with degraded coatings tend to accumulate in Kupffer cells, whereas those with intact coatings are more frequently found in hepatocytes. In comparison to previous reports, we further examined subhepatic uptake of nanoparticles to suggest the potential for more elimination via the hepatobiliary system at longer time points. In summary, we demonstrated that different synthetic conditions could lead to very different outcomes in terms of material properties and in vivo performance relationships. As informed by our results, it is important to perform in-depth characterization to accurately describe the nature of the as-synthesized nanomaterials and fully understand their subsequent behaviors at the nanobiointerface. It is also important to examine synthetic designs that impact nanoparticle clearance and biodistribution profiles.

Supplementary Material

Refer to Web version on PubMed Central for supplementary material.

ACKNOWLEDGMENTS

This material was based upon work supported by the National Science Foundation Graduate Research Fellowship under Grant No. DGE-1321851 and the Brody Family Medical Trust Fund Fellowship in “Incurable Diseases” of The Philadelphia Foundation (both to J.C.H.). Partial support was provided by an NIH grant R01-CA227142 (D.P.C.), a Franco-American Commission Fulbright Fellowship (M.B.), and the Center for Engineering MechanoBiology (CEMB), an NSF Science and Technology Center, under grant agreement CMMI: 15-48571 (Y.D.). This work was carried out in part at the Singh Center for Nanotechnology, part of the National Nanotechnology Coordinated Infrastructure Program, which is supported by the National Science Foundation grant NNCI-1542153.

REFERENCES

(1). Dong YC; Hajfathalian M; Maidment PSN; Hsu JC; Naha PC; Si-Mohamed S; Breuilly M; Kim J; Chhour P; Douek P; Litt HI; Cormode DP Effect of gold nanoparticle size on their properties as contrast agents for computed tomography. Sci. Rep 2019, 9, 14912. [PubMed: 31624285]

(2). Bouché M; Hsu JC; Dong YC; Kim J; Taing K; Cormode DP Recent advances in molecular imaging with gold nanoparticles. Bioconjugate Chem. 2020, 31, 303–314.

(3). Naha PC; Lau KC; Hsu JC; Hajfathalian M; Mian S; Chhour P; Uppuluri L; McDonald ES; Maidment AD; Cormode DP Gold silver alloy nanoparticles (GSAN): an imaging probe for breast cancer screening with dual-energy mammography or computed tomography. Nanoscale 2016, 8, 13740–13754. [PubMed: 27412458]

(4). Si-Mohamed SA; Sigovan M; Hsu JC; Tatard-Leitman V; Chalabreysse L; Naha PC; Garrivier T; Dessouky R; Carnaru M; Boussel L; Cormode DP; Douek PC In vivo molecular k-edge imaging of atherosclerotic plaque using photon-counting CT. Radiology 2021, 300, 98. [PubMed: 33944628]

(5). Nieves LM; Hsu JC; Lau KC; Maidment ADA; Cormode DP Silver telluride nanoparticles as biocompatible and enhanced contrast agents for X-ray imaging: an in vivo breast cancer screening study. Nanoscale 2021, 13, 163–174. [PubMed: 33325953]

(6). de Jong WH; Hagens WI; Krystek P; Burger MC; Sips AJAM; Geertsma RE Particle size-dependent organ distribution of gold nanoparticles after intravenous administration. Biomaterials 2008, 29, 1912–1919. [PubMed: 18242692]

(7). Soo Choi H; Liu W; Misra P; Tanaka E; Zimmer JP; Itty Ipe B; Bawendi MG; Frangioni JV Renal clearance of quantum dots. Nat. Biotechnol 2007, 25, 1165–1170. [PubMed: 17891134]

(8). Zhou C; Long M; Qin Y; Sun X; Zheng J Luminescent gold nanoparticles with efficient renal clearance. Angew. Chem., Int. Ed. Engl 2011, 50, 3168–3172. [PubMed: 21374769]

(9). Hainfeld JF; Slatkin DN; Focella TM; Smilowitz HM Gold nanoparticles: A new X-ray contrast agent. Br. J. Radiol 2006, 79, 248–253. [PubMed: 16498039]

(10). FitzGerald PF; Butts MD; Roberts JC; Colborn RE; Torres AS; Lee BD; Yeh BM; Bonitatibus PJ Jr. A proposed computed tomography contrast agent using carboxybetaine zwitterionic tantalum oxide nanoparticles: Imaging, biological, and physicochemical performance. Invest. Radiol 2016, 51, 786–796. [PubMed: 27115702]

(11). Menon MC; Chuang PY; He CJ The glomerular filtration barrier: Components and crosstalk. Int. J. Nephrol 2012, 2012, No. 749010.

(12). Hsu JC; Nieves LM; Betzer O; Sadan T; Noel PB; Popovtzer R; Cormode DP Nanoparticle contrast agents for X-ray imaging applications. Wiley Interdiscip Rev: Nanomed. Nanobiotechnol 2020, 12, No. e1642.

(13). Hsu JC; Cruz ED; Lau KC; Bouché M; Kim J; Maidment ADA; Cormode DP Renally excretable and size-tunable silver sulfide nanoparticles for dual-energy mammography or computed tomography. Chem. Mater 2019, 31, 7845–7854. [PubMed: 33005070]

(14). Du B; Yu M; Zheng J Transport and interactions of nanoparticles in the kidneys. Nat. Rev. Mater 2018, 3, 358–374.

(15). Zhang Y; Zhang Y; Hong G; He W; Zhou K; Yang K; Li F; Chen G; Liu Z; Dai H; Wang Q Biodistribution, pharmacokinetics and toxicology of Ag_2S near-infrared quantum dots in mice. Biomaterials 2013, 34, 3639–3646. [PubMed: 23415643]

(16). Yang L; Kuang H; Zhang W; Aguilar ZP; Wei H; Xu H Comparisons of the biodistribution and toxicological examinations after repeated intravenous administration of silver and gold nanoparticles in mice. Sci. Rep 2017, 7, 3303. [PubMed: 28607366]

(17). Kang H; Gravier J; Bao K; Wada H; Lee JH; Baek Y; El Fakhri G; Gioux S; Rubin BP; Coll JL; Choi HS Renal clearable organic nanocarriers for bioimaging and drug delivery. Adv. Mater 2016, 28, 8162–8168. [PubMed: 27414255]

(18). Kim J; Silva AB; Hsu JC; Maidment PSN; Shapira N; Noäl PB; Cormode DP Radioprotective garment-inspired biodegradable polymetal nanoparticles for enhanced CT contrast production. Chem. Mater 2020, 32, 381–391. [PubMed: 33005071]

(19). Cheheltani R; Ezzibdeh RM; Chhour P; Pulaparthi K; Kim J; Jurcova M; Hsu JC; Blundell C; Litt HI; Ferrari VA; Allcock HR; Sehgal CM; Cormode DP Tunable, biodegradable gold nanoparticles as contrast agents for computed tomography and photoacoustic imaging. Biomaterials 2016, 102, 87–97. [PubMed: 27322961]

(20). Bouché M; Pühringer M; Iturmendi A; Amirshaghaghi A; Tsourkas A; Teasdale I; Cormode DP Activatable hybrid polyphosphazene-AuNP nanoprobe for ROS detection by bimodal PA/CT imaging. ACS Appl. Mater. Interfaces 2019, 11, 28648–28656. [PubMed: 31321973]

(21). Aparicio-Vergara M; Tencerova M; Morgantini C; Barreby E; Aouadi M Isolation of kupffer cells and hepatocytes from a single mouse liver. Methods Mol. Biol 2017, 1639, 161–171. [PubMed: 28752456]

(22). Du Y; Li N; Yang H; Luo C; Gong Y; Tong C; Gao Y; Lü S; Long M Mimicking liver sinusoidal structures and functions using a 3D-configured microfluidic chip. Lab Chip 2017, 17, 782–794. [PubMed: 28112323]

(23). Wu Q; Cao H; Zhang S; Zhang X; Rabinovich D Generation and optical properties of monodisperse wurtzite-type ZnS microspheres. Inorg. Chem 2006, 45, 7316–7322. [PubMed: 16933933]

(24). Panigrahi S; Kundu S; Basu S; Praharaj S; Jana S; Pande S; Ghosh SK; Pal A; Pal T Cysteine functionalized copper organosol: synthesis, characterization and catalytic application. Nanotechnology 2006, 17, 5461–5468.

(25). Shankar R; Kolandaivel P; Senthil Kumar L Coordination and binding properties of zwitterionic glutathione with transition metal cations. Inorg. Chim. Acta 2012, 387, 125–136.

(26). Mandal S; Gole A; Lala N; Gonnade R; Ganvir V; Sastry M Studies on the reversible aggregation of cysteine-capped colloidal silver particles interconnected via hydrogen bonds. Langmuir 2001, 17, 6262–6268.

(27). Burford N; Eelman MD; Mahony DE; Morash M Definitive identification of cysteine and glutathione complexes of bismuth by mass spectrometry: assessing the biochemical fate of bismuth pharmaceutical agents. Chem. Commun 2003, 1, 146–147.

(28). Siva C; Iswarya CN; Baraneedharan P; Sivakumar M L-Cysteine assisted formation of mesh like Ag_2S and Ag_3AuS_2 nanocrystals through hydrogen bonds. Mater. Lett 2014, 134, 56–59.

(29). Xiang J; Cao H; Wu Q; Zhang S; Zhang X; Watt AAR L-cysteine-assisted synthesis and optical properties of Ag_2S nanospheres. J. Phys. Chem. C 2008, 112, 3580–3584.

(30). Zhang B; Ye X; Dai W; Hou W; Xie Y Biomolecule-assisted synthesis and electrochemical hydrogen storage of porous spongelike Ni_3S_2 nanostructures grown directly on nickel foils. Chemistry 2006, 12, 2337–2342. [PubMed: 16389618]

(31). Feng B; Zhu R; Xu S; Chen Y; Di J A sensitive LSPR sensor based on glutathione-functionalized gold nanoparticles on a substrate for the detection of Pb^{2+} ions. RSC Adv. 2018, 8, 4049–4056.

(32). Stroock AD; Dertinger SK; Ajdari A; Mezić I; Stone HA; Whitesides GM Chaotic mixer for microchannels. Science 2002, 295, 647–651. [PubMed: 11809963]

(33). Brelle MC; Zhang JZ; Nguyen L; Mehra RK Synthesis and ultrafast study of cysteine- and glutathione-capped Ag_2S semiconductor colloidal nanoparticles. J. Phys. Chem. A 1999, 103, 10194–10201.

(34). Hocaoglu I; Çizmeciyan MN; Erdem R; Ozen C; Kurt A; Sennaroglu A; Acar HY Development of highly luminescent and cytocompatible near-IR-emitting aqueous Ag_2S quantum dots. J. Mater. Chem 2012, 22, 14674–14681.

(35). Yang T; Tang Y; Liu L; Lv X; Wang Q; Ke H; Deng Y; Yang H; Yang X; Liu G; Zhao Y; Chen H Size-dependent Ag_2S nanodots for second near-infrared fluorescence/photoacoustics imaging and simultaneous photothermal therapy. ACS Nano 2017, 11, 1848–1857. [PubMed: 28117993]

(36). Leung BO; Jalilehvand F; Mah V; Parvez M; Wu Q Silver(I) complex formation with cysteine, penicillamine, and glutathione. Inorg. Chem 2013, 52, 4593–4602. [PubMed: 23556419]

(37). Qian H; Zhu M; Gayathri C; Gil RR; Jin R Chirality in gold nanoclusters probed by NMR spectroscopy. ACS Nano 2011, 5, 8935–8942. [PubMed: 21981416]

(38). Guo C; Yarger JL Characterizing gold nanoparticles by NMR spectroscopy. Magn. Reson. Chem 2018, 56, 1074–1082. [PubMed: 29808623]

(39). Farrag M Preparation, characterization and photocatalytic activity of size selected platinum nanoclusters. J. Photochem. Photobiol., A 2016, 318, 42–50.

(40). Hsu JC; Naha PC; Lau KC; Chhour P; Hastings R; Moon BF; Stein JM; Witschey WRT; McDonald ES; Maidment ADA; Cormode DP An all-in-one nanoparticle (AION) contrast agent for breast cancer screening with DEM-CT-MRI-NIRF Imaging. Nanoscale 2018, 10, 17236–17248. [PubMed: 30191237]

(41). Charni-Natan M; Goldstein I Protocol for primary mouse hepatocyte isolation. STAR Protoc. 2020, 1, No. 100086.

(42). Racanelli V; Rehermann B The liver as an immunological organ. Hepatology 2006, 43, S54–S62. [PubMed: 16447271]

(43). Campbell ZS; Bateni F; Volk AA; Abdel-Latif K; Abolhasani M Microfluidic synthesis of semiconductor materials: Toward accelerated materials development in flow. Part. Part. Syst. Charact 2020, 37, No. 2000256.

(44). Shepherd SJ; Issadore D; Mitchell MJ Microfluidic formulation of nanoparticles for biomedical applications. Biomaterials 2021, 274, No. 120826.

(45). Zhang YN; Poon W; Tavares AJ; McGilvray ID; Chan WCW Nanoparticle-liver interactions: Cellular uptake and hepatobiliary elimination. J. Controlled Release 2016, 240, 332–348.

(46). Tsoi KM; MacParland SA; Ma XZ; Spetzler VN; Echeverri J; Ouyang B; Fadel SM; Sykes EA; Goldaracena N; Kaths JM; Conneely JB; Alman BA; Selzner M; Ostrowski MA; Adeyi OA; Zilman A; McGilvray ID; Chan WC Mechanism of hard-nanomaterial clearance by the liver. Nat. Mater. 2016, 15, 1212–1221. [PubMed: 27525571]

(47). Cheng SH; Li FC; Souris JS; Yang CS; Tseng FG; Lee HS; Chen CT; Dong CY; Lo LW Visualizing dynamics of sub-hepatic distribution of nanoparticles using intravital multiphoton fluorescence microscopy. ACS Nano 2012, 6, 4122–4131. [PubMed: 22486639]

(48). Cormode DP; Skajaa GO; Delshad A; Parker N; Jarzyna PA; Calcagno C; Galper MW; Skajaa T; Briley-Saebo KC; Bell HM; Gordon RE; Fayad ZA; Woo SL; Mulder WJ A versatile and tunable coating strategy allows control of nanocrystal delivery to cell types in the Liver. Bioconjugate Chem. 2011, 22, 353–361.

(49). Akinc A; Querbes W; de S; Qin J; Frank-Kamenetsky M; Jayaprakash KN; Jayaraman M; Rajeev KG; Cantley WL; Dorkin JR; Butler JS; Qin L; Racie T; Sprague A; Fava E; Zeigerer A; Hope MJ; Zerial M; Sah DW; Fitzgerald K; Tracy MA; Manoharan M; Koteliansky V; Fougerolles A; Maier MA Targeted delivery of RNAi therapeutics with endogenous and exogenous ligand-based mechanisms. Mol. Ther 2010, 18, 1357–1364. [PubMed: 20461061]

(50). Yamada T; Iwasaki Y; Tada H; Iwabuki H; Chuah MK; VandenDriessche T; Fukuda H; Kondo A; Ueda M; Seno M; Tanizawa K; Kuroda S Nanoparticles for the delivery of genes and drugs to human hepatocytes. Nat. Biotechnol 2003, 21, 885–890. [PubMed: 12833071]

(51). Bergen JM; von Recum HA; Goodman TT; Massey AP; Pun SH Gold nanoparticles as a versatile platform for optimizing physicochemical parameters for targeted drug delivery. Macromol. Biosci 2006, 6, 506–516. [PubMed: 16921538]

(52). Walkey CD; Olsen JB; Guo H; Emili A; Chan WCW Nanoparticle size and surface chemistry determine serum protein adsorption and macrophage uptake. J. Am. Chem. Soc 2012, 134, 2139–2147. [PubMed: 22191645]

(53). Poelstra K; Prakash J; Beljaars L Drug targeting to the diseased liver. J. Controlled Release 2012, 161, 188–197.

(54). Bartsch M; Weeke-Klimp AH; Meijer DK; Scherphof GL; Kamps JA Massive and selective delivery of lipid-coated cationic lipoplexes of oligonucleotides targeted in vivo to hepatic endothelial cells. Pharm. Res 2002, 19, 676–680. [PubMed: 12069172]

(55). Sadauskas E; Danscher G; Stoltenberg M; Vogel U; Larsen A; Wallin H Protracted elimination of gold nanoparticles from mouse liver. Nanomedicine 2009, 5, 162–169. [PubMed: 19217434]

(56). Balasubramanian SK; Jittiwat J; Manikandan J; Ong CN; Yu LE; Ong WY Biodistribution of gold nanoparticles and gene expression changes in the liver and spleen after intravenous administration in rats. Biomaterials 2010, 31, 2034–2042. [PubMed: 20044133]

(57). Nieves LM; Mossburg K; Hsu JC; Maidment ADA; Cormode DP Silver chalcogenide nanoparticles: a review of their biomedical applications. Nanoscale 2021, DOI: 10.1039/D0NR03872E.

(58). Jiang X; Du B; Zheng J Glutathione-mediated biotransformation in the liver modulates nanoparticle transport. Nat. Nanotechnol 2019, 14, 874–882. [PubMed: 31308501]

(59). Walton K; Dorne JLCM; Renwick AG Species-specific uncertainty factors for compounds eliminated principally by renal excretion in humans. Food Chem. Toxicol 2004, 42, 261–274. [PubMed: 14667472]

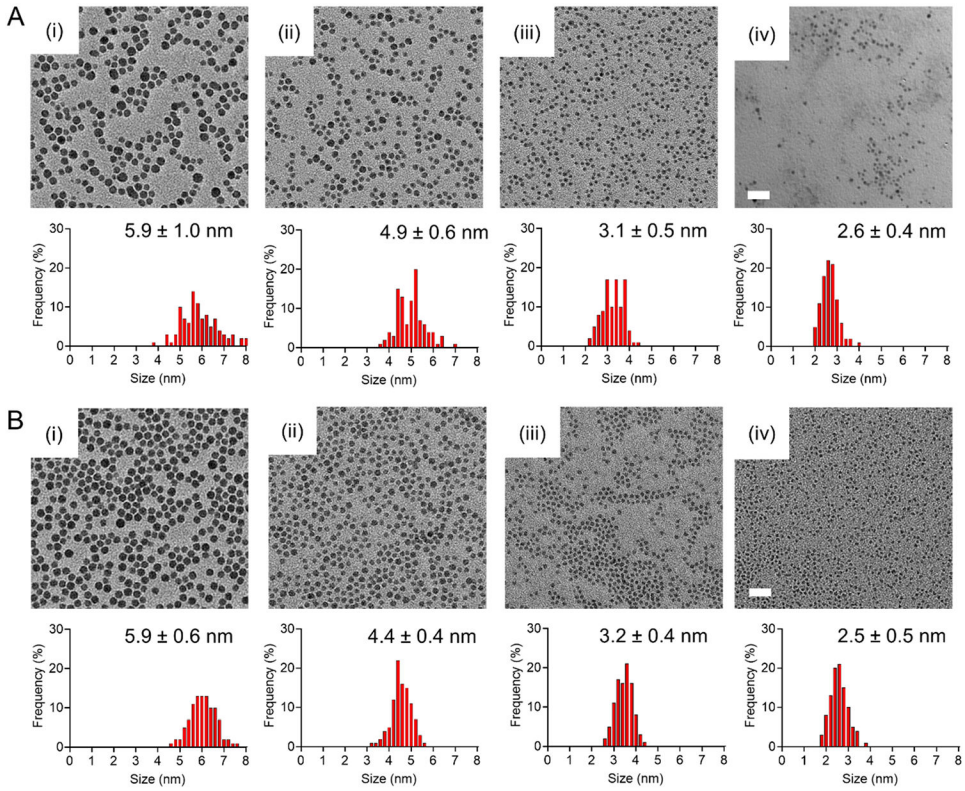

Figure 1.

Electron micrographs and core size distributions of Ag_2S-NPs formed under two different synthetic conditions. (A) Synthesis A involves heating of molecular precursors and quenching the reaction at (i) 17, (ii) 15, (iii) 13, and (iv) 11 min to obtain Ag_2S-NPs with the core sizes shown. (B) Synthesis B involves mixing of precursors through a microfluidic chip at room temperature and setting the combined flow rate at (i) 1, (ii) 1.5, (iii) 2, and (iv) 3 mL/min to obtain Ag_2S-NPs with the core sizes shown. The scale is indicated in the bottom left corner on the rightmost image for each row of images. Scale bar = 20 nm.

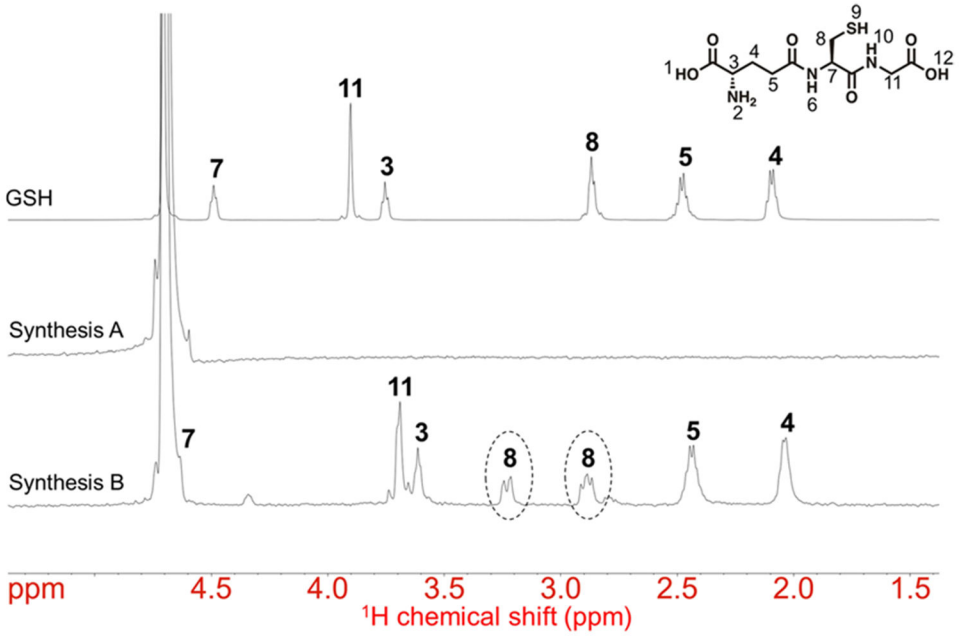

Figure 2.

^{1}H NMR spectra of glutathione and the as-synthesized Ag_2S-NPs.

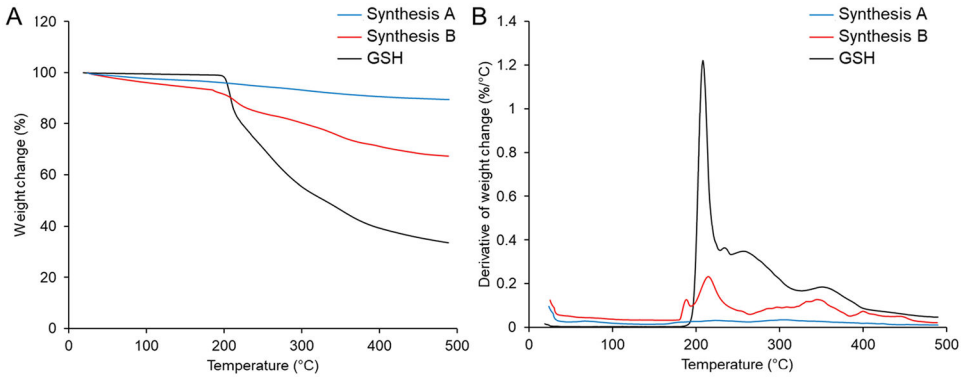

Figure 3.

TGA spectra of glutathione and the as-synthesized Ag_2S-NPs. The change in (A) weight (%) and (B) weight change (%/°C) of various samples as the temperature increases to 500 °C.

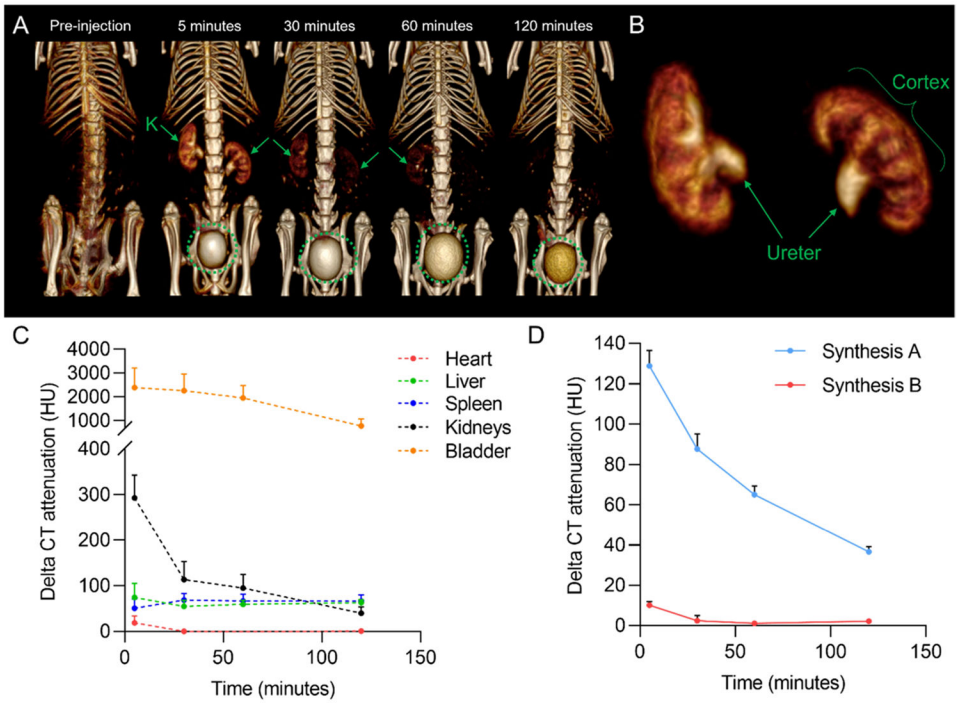

Figure 4.

In vivo CT imaging data for Ag_2S-NPs synthesized using microfluidics. (A) Representative CT images of a mouse after injection using 3D volume rendering. The images are shown with a window level of 700 HU and a window width of 1000 HU. Kidneys are labeled K. Green circles indicate the bladder. (B) 3D region growing segmentation of mouse kidneys at 5 min post-injection to visualize glomerular filtration and collection of Ag_2S-NPs into the bladder via the ureter. (C) Change in CT attenuation in various organs of mice compared to preinjection. (D) Change in CT attenuation in the blood of mice compared to preinjection. Error bars are SEM ($n = 4$).

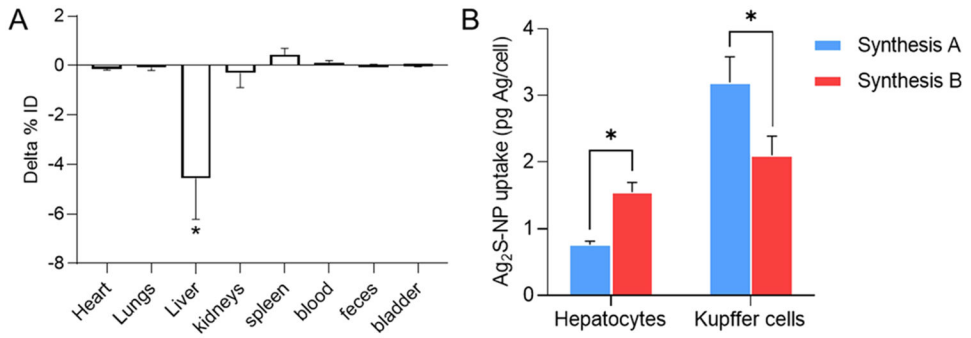

Figure 5.

Biodistribution and hepatic cellular distribution of the as-synthesized Ag_2S-NPs. (A) Difference in silver content in major organs at 24 h after injection. Delta % ID = % ID of Ag_2S-NPs from Synthesis B – % ID of Ag_2S-NPs from Synthesis A. (B) Distribution of different Ag_2S-NP formulations in hepatocytes and Kupffer cells. Error bars are SEM (n = 4). * indicates $P < 0.05$ (two-way ANOVA with Bonferroni's multiple comparison test).